RNA-dependent RNA polymerase of predominant human norovirus forms liquid-liquid phase condensates as viral replication factories

Soni Kaundal[1], Ramakrishnan Anish [1], B. Vijayalakshmi Ayyar[2], Sreejesh Shanker[1], Gundeep Kaur[3], Sue E. Crawford[2], Jeroen Pollet[4], Fabio Stossi[5], Mary K. Estes[2,6], B.V. Venkataram Prasad[1,2]*

Affiliations:

[1]Department of Biochemistry and Molecular Pharmacology Baylor College of Medicine, Houston, Texas, U.S.A.

[2]Department of Molecular Virology and Microbiology, Baylor College of Medicine, Houston, Texas, U.S.A.

[3]Department of Epigenetics and Molecular Carcinogenesis, The University of Texas, MD Anderson Cancer Center, Houston, Texas U.S.A.

[4]Department of Pediatrics-Tropical Medicine Baylor College of Medicine, Houston, Texas, U.S.A.

[5]Department of Molecular and Cellular Biology, Baylor College of Medicine, Houston, Texas, U.S.A.

[6]Department of Medicine, Baylor College of Medicine, Houston, Texas, U.S.A.

* Corresponding author: B. V. Venkataram Prasad, E-mail: vprasad@bcm.edu

Abstract

Many viral proteins form biomolecular condensates via liquid-liquid phase separation (LLPS) to support viral replication and evade host antiviral responses, and thus, they are potential targets for designing antivirals. In the case of non-enveloped positive-sense RNA viruses, forming such condensates for viral replication is unclear and less understood. Human noroviruses (HuNoV) are positive-sense RNA viruses that cause epidemic and sporadic gastroenteritis worldwide. Here, we show that the RNA-dependent-RNA polymerase (RdRp) of pandemic GII.4 HuNoV forms distinct condensates that exhibit all the signature properties of LLPS with sustained polymerase activity and the capability of recruiting components essential for viral replication. We show that such condensates are formed in HuNoV-infected human intestinal enteroid cultures and are the sites for genome replication. Our studies demonstrate the formation of phase separated condensates as replication factories in a positive-sense RNA virus, which plausibly is an effective mechanism to

dynamically isolate RdRp replicating the genomic RNA from interfering with the ribosomal translation of the same RNA.

Teaser

How liquid-liquid phase separation fuels viral replication in human noroviruses

Introduction

The compartmentalization of biomolecules is essential for efficiently regulating numerous biological processes in a densely packed cellular environment. A wealth of new research has shown that, apart from the traditional membrane-bound organelles, eukaryotic cells also contain membraneless organelles such as P granules, nucleoli, Cajal bodies, etc. [1-3]. These membraneless organelles, also known as biomolecular condensates, are formed by the process of liquid-liquid phase separation (LLPS), where a single, uniform liquid phase separates into a dense phase that coexists with the surrounding dilute phase [4, 5]. These condensates, often initiated by a single protein, selectively allow the incorporation of proteins and nucleic acids to provide exclusive compartments for performing specialized cellular functions, including gene regulation, protein synthesis, and signaling [5, 6]. Depending upon the sequence and concentration of the protein, the presence of other biomolecules, and the physiochemical properties of the surroundings, the dense phase can have the material properties of a liquid, gel, or solid [3, 7, 8]. The liquid-like condensates typically have a spherical shape with a dynamic interior and exhibit the ability to fuse with each other, deform upon physical contact, and revert to the spherical shape [3, 8]. Signature features of the proteins undergoing LLPS include the presence of a nucleic acid binding domain, a disordered/flexible region, a low complexity region, and the ability to form oligomers [9, 10].

Many viruses, upon infecting host cells, form distinct intracellular compartments, often referred to as viroplasms or replication factories (RFs), for genome replication and capsid assembly [11, 12]. In negative-sense RNA and dsRNA viruses, these compartments are typically membraneless organelles within the cytoplasm, commonly known as inclusion bodies. A growing amount of evidence shows that these inclusion bodies have liquid-like properties. The formation of liquid condensates by viral proteins (N and P) was initially demonstrated for Mononegavirales with negative-strand RNA genome, including rabies virus [13], vesicular stomatitis virus [14], measles virus [15], and respiratory syncytial virus [16]. In the case of rotavirus, a dsRNA virus, non-structural protein NSP5, in association with the NSP2 protein, undergoes LLPS to form viroplasms, the sites for viral replication[17]. In contrast, the viral replication complexes of positive-sense RNA viruses are associated with modified cellular membranes [18, 19]. However, recent research has demonstrated that proteins encoded by positive-sense RNA viruses can also exhibit phase

separation behavior and play a critical role in the viral life cycle. For example, phase separation by the N protein of SARS-CoV2 is implicated in virus replication, genome packaging, and immune suppression [20-25]. This implies that other positive-sense RNA viruses likely depend on crucial proteins for phase separation to control replication, and discovering these proteins could pave the way for novel and improved drug therapies.

Apart from the N protein of SARS-CoV2, there are very limited reports of proteins encoded by other positive-sense RNA viruses proteins undergoing phase separation [26], particularly in the context of their replication. Here, we investigated the phase separation behavior of protein (s) encoded by human norovirus (HuNoV), a positive-sense RNA virus. HuNoVs are the leading cause of viral gastroenteritis and pose a significant global health and economic burden without any approved vaccines or antivirals [27, 28]. These icosahedral, single-stranded RNA viruses, belonging to the *Norovirus* genus in the *Caliciviridae* family account for an estimated ~685 million cases and ~212,000 deaths globally per year with an economic impact of $60 billion [27-31]. The NoVs are classified into at least 10 genogroups (GI-GX) and 49 genotypes [32]. NoVs in genogroups GI, GII, GIV, GVIII, and GIX infect humans [32, 33], and among these, HuNoVs belonging to genogroup II and genotype 4 (GII.4) are responsible for ~80 % of the outbreaks worldwide [34]. The NoV genome is covalently linked to VPg and consists of three open reading frames (ORFs). ORF1 encodes a polyprotein that is cleaved into six nonstructural proteins by the viral protease to produce p48 (NS1-2), p41 (NS3), p22 (NS4), VPg (NS5), protease (NS6), and the RNA-dependent RNA polymerase (RdRp) (NS7) [35]. ORF2 and ORF3 encode the major capsid protein VP1 and a minor structural protein VP2, respectively [36]. Our understanding of the HuNoV replication processes in infected cells has been hampered by the lack of a robust cell culture system. Much of our current understanding of the entry and replication processes of HuNoVs has come from using the human intestinal stem cell-derived, nontransformed enteroid (HIE) monolayer cultures [37-39] for virus cultivation.

Using bioinformatics analysis, we found that among the nonstructural proteins encoded by the pandemic GII.4 Sydney strain, RdRp has the highest propensity to undergo LLPS to form biomolecular condensates. In addition to the biophysical proprieties of GII.4 RdRp, such as its modular architecture, the presence of an N-terminal disordered/flexible region, the ability to homo-oligomerize and bind RNA, and the critical role it plays during viral replication prompted us to experimentally test the hypothesis that GII.4 RdRp drives the formation of biomolecular condensates that are conducive for viral replication through LLPS. Our studies show that RdRp, consistent with its biophysical properties, indeed forms highly dynamic liquid-like condensates via

79 LLPS at physiologically relevant conditions and that the disordered/flexible N-terminal region of
80 RdRp is critical for LLPS. Our studies further show that distinct puncta observed in the virus-
81 infected HIEs are liquid-like condensates representing replication compartments, as evidenced by
82 the presence of RdRp, replication intermediate dsRNA, and nonstructural protein (VPg). Together,
83 these findings establish that HuNoV RdRp undergoes LLPS to form biomolecular condensates,
84 which serve as efficient platforms for viral replication.
85

86 **Results**

87 **HuNoV RdRp exhibits the obligatory properties to undergo LLPS**

88 We used the DeePhase server [40] to analyze the primary amino acid sequences of all the
89 nonstructural proteins encoded by HuNoV GII.4 (Sydney) for their ability to undergo LLPS (Fig.
90 1A). This analysis predicted that RdRp, with an overall score of 0.67, has the highest propensity to
91 undergo LLPS. The known biochemical and enzymatic properties of RdRp are consistent with this
92 prediction. As a protein critical for the transcription and replication of genomic RNA, the RNA
93 binding property of RdRp satisfies one of the essential criteria for undergoing LLPS. Other
94 requirements include the presence of disordered or flexible regions and the ability to form higher-
95 order oligomers. Analysis by PONDR (Fig. 1B) [41] and IUPred2 (Fig. 1C) [42] software shows
96 the presence of disordered N-terminal ~50 residues in RdRp.

97 To experimentally confirm the LLPS driving properties of GII.4 RdRp, we purified
98 recombinant RdRp and determined its oligomeric state using size exclusion chromatography (SEC)
99 (Fig. 1D) and sedimentation velocity analytical ultracentrifugation (SV-AUC) (Fig. 1E) which
100 show that while most of the RdRp (75 %) exists as a monomer in physiologically relevant
101 conditions, a fraction of it also tends to form dimers (15 %) and higher-order oligomers. We also
102 determined the X-ray crystal structure of RdRp at 2.0 Å resolution using molecular replacement
103 (PDB ID: 8TUF, Supplementary Table 1). The crystal structure shows, as expected, all the features
104 observed in the previous crystallographic structures of the NoV RdRps [43-46], with a polypeptide
105 fold resembling a partially closed right hand, with fingers, thumb, and palm as subdomains (Fig.
106 1F). The N-terminal 50 residues with only two small stretches of β-stands form a flap connecting
107 the finger and the thumb domains. To visualize the possible flexible regions in the RdRp, we
108 performed Size Exclusion Chromatography coupled to Small Angle X-ray Scattering (SEC-SAXS)
109 studies combined with molecular dynamics simulations using BILBOMD [47]. Guinier plot
110 analysis suggests that purified RdRp does not show any signs of aggregation and has radius of
111 gyration (R_g) ~25 Å (Fig. S1A and B). Kratky plot shows that RdRp is globular in shape and exists

112 as a monomer in solution (Fig. S1C), and the P(r) plot shows that RdRp is ~70 Å in diameter (D_{max})
113 (Fig. S1D). To model the population of different conformations adopted by RdRp in solution, we
114 used the X-ray structure of RdRp as the template and generated an ensemble of molecular models
115 (~10,000) varying in R_g and D_{max} (Fig. S1E) and the topmost models with χ^2 close to 1 were further
116 used for calculating theoretical SAXS curves. The experimental scattering profile obtained from
117 purified RdRp was compared to the theoretical scattering profiles of top 8 BILBOMD atomistic
118 models (Fig. S1E). We superposed the shortlisted BILBOMD models to the experimentally
119 determined crystal structure of RdRp and observed that fingers, thumb, and palm domains of
120 BILBOMD models superpose well (rmsd: 1.05 Å over 465 Cα atoms) except the N-terminal 50
121 residues which appear to adopt a wide range of orientations in the solution (Fig. S1F) indicating its
122 flexible nature. Together, these studies suggest that RdRp is a suitable candidate to further
123 investigate its phase separation behavior.

124 **HuNoV RdRp undergoes phase separation to form dynamic liquid-like condensates**

125 To experimentally validate that RdRp undergoes LLPS, we studied its phase separation
126 behavior in vitro using light scattering experiments and confocal microscopy. Under physiological
127 conditions, the homogeneously mixed purified RdRp (10 μM) phase separates to form a demixed
128 turbid solution when incubated at 37 °C for 45 min (Fig. S2). The presence of condensates in the
129 phase separated solution was examined by confocal microscopy using a mixture of Atto 488-labeled
130 (1 %) and unlabeled (99 %) RdRp using depression slides. The micrographs showed the formation
131 of distinct spherical condensates (Fig. 2A). We examined the liquid-like nature of these condensates
132 by assessing their sensitivity towards the aliphatic alcohol 1,6-hexanediol (1,6 HD), which is
133 commonly used as a chemical probe to distinguish between liquid-like and gel-like states of
134 biomolecular condensates [48, 49]. The 1,6 HD (5%) treatment shows the dissolution of
135 condensates, indicating their liquid-like nature (Fig. 2B). Further, we investigated the dynamic
136 nature of these condensates using fluorescence recovery after photobleaching (FRAP) of the RdRp
137 molecules in the condensates. We observed a complete fluorescence recovery (98 %) with a half-
138 life ($t_{1/2}$) of 53.3 ± 2.1 s (Fig. 2C, D and Supplementary Video 1) indicating diffusion of RdRp
139 molecules in the condensate. Using time-lapse confocal microscopy, we observed that smaller
140 RdRp condensates fuse to form a larger condensate (Fig. 2E and Supplementary Video 2) and
141 undergo surface wetting and dripping (Fig. 2F). Our studies thus clearly show that HuNoV GII.4
142 RdRp undergoes phase separation to form dynamic, liquid-like condensates, which are dense and
143 high in RdRp concentration yet allow the RdRp molecules to move freely within the condensates
144 and exchange with the surrounding environment.

145 **Molecular crowding, pH and salt concentration modulate phase separation properties of**
146 **HuNoV GII.4 RdRp**

147 To examine whether there is a minimum concentration of RdRp necessary to undergo LLPS,
148 and how this concentration is affected by molecular crowding agents such as polyethylene glycol
149 (PEG), typically used to simulate intracellular molecular crowding, we used two different
150 techniques: light scattering experiments to measure turbidity (Fig. 3A) and confocal microscopy to
151 assess LLPS formation (Fig. 3D). Different concentrations (0.5-25 μM) of RdRp were screened
152 with and without PEG3350 (5-20 %). Confocal microscopy results suggest the minimum
153 concentration for phase separation of RdRp decreases from 5 μM to 0.5 μM by adding 10 %
154 PEG3350. The results show that an increase in molecular crowding, as expected inside the cells
155 during virus replication, decreases the minimum concentration of the protein to phase separate. Our
156 light scattering experiments with PEG3350 also supported this result (Fig. 3A).

157 As it has been shown that virus infection can alter the intracellular pH and salt
158 concentrations of the host cell [50-52], we further examined if these factors can affect the phase
159 separation behavior of RdRp. We observed increased turbidity in the purified RdRp at an acidic pH
160 of 5.5 compared to a neutral pH, indicating that an acidic pH promotes phase separation more
161 effectively than a neutral pH. In contrast, the turbidity was significantly less at an alkaline pH of
162 9.0 (Fig. 3B). Since turbidity measurement is affected by the condensate's size, shape, and density,
163 we further performed confocal microscopy at different pH conditions (Fig. 3E). RdRp forms larger
164 condensates at pH 5.5 than at pH 7.5, and, at pH 9, the condensates are few and have an irregular
165 shape. In addition, at pH 5.5, the minimum concentration of RdRp required to form LLPS decreased
166 to 0.5 μM from 5 μM at pH 7.5. Since the predicted pI of RdRp is 6.16, these observations suggest
167 that positive charges from basic residues in RdRp are critical for promoting phase separation.

168 We also tested the effect of ionic strength on the phase separation of RdRp by measuring
169 the turbidity of the solutions containing varying concentrations of NaCl using turbidity
170 measurements at 350 nm (Fig. 3C), and by imaging the condensates using confocal microscopy
171 (Fig. 3F). These studies showed GII.4 RdRp undergoes phase separation at NaCl concentrations
172 between 10-500 mM. The low ionic strength enhances protein-protein electrostatic or π-π
173 interactions, whereas high salt abolishes these interactions. Recent studies have shown a similar
174 behavior of the N protein of SARS-CoV-2 concerning pH and ionic strength [23].

175 **The flexible N-terminal region is critical for HuNoV GII.4 RdRp LLPS**

176 To validate the predicted role of the flexible N-terminal region of RdRp in forming the
177 condensates, first, we analyze the N-terminal deletion protein, HuNoV GII.4 RdRp-NΔ51 using

178 DeePhase [40]. This analysis shows that the deletion of N-terminal 51 residues reduces the
179 DeePhase score (Fig. S3A). Analysis of RdRp using ParSe [53], another bioinformatics tool to
180 predict the amino acid involved in LLPS, suggests that the N-terminal region of RdRp plays an
181 important role in LLPS (Fig. S3B). We expressed and purified RdRp-NΔ51 and investigated if this
182 protein is properly folded and enzymatically active. The CD spectra of RdRp wild type (WT) and
183 RdRp-NΔ51 showed two distinct negative maxima at λ = 208 nm and 220 nm and a strong positive
184 peak around 190 nm indicative of an α-helical conformation and thus of proper folding of the N-
185 terminal deletion construct (Fig. 4A). We also assessed the RNA polymerization activity of RdRp-
186 NΔ51 protein with a fluorescence-based assay using SYTO9 dye used in many recent studies [54,
187 55]. The results indicate that RdRp-NΔ51 is enzymatically active with comparable activity with
188 RdRp WT (Fig. 4B and C, respectively). Size exclusion chromatography of this deletion construct
189 shows a reduction in their ability to form oligomers (Fig. 4D). Confocal microscopy images show
190 that deletion of N-terminal 51 residues (RdRp-NΔ51), which includes 5 aromatic residues, showed
191 few and very small condensates that were difficult to image compared to RdRp WT (Fig. 4E).
192 Together these results clearly demonstrate that flexible N-terminal region of RdRp plays a critical
193 role in its phase separation behavior.

194 **RdRp is enzymatically active within liquid condensates**

195 We estimated the concentration of RdRp in the condensates using the centrifugation method
196 [56]which shows that it is ~20 times higher than the surrounding dilute phase. To examine if the
197 highly concentrated protein in the condensate is enzymatically active, we monitored the formation
198 of dsRNA from an ssRNA template using a well-established fluorescence-based assay in which the
199 fluorescent dye SYTO9 binds specifically to dsRNA and fluoresces when excited at 485 nm [54,
200 55] using a Yokogawa CV8000 high throughput spinning disk confocal microscope. Analysis of
201 time-lapse images shows an increase in fluorescence intensity within the condensates over time,
202 suggesting the formation of dsRNA and, thus, the activity of RdRp (Fig. S4).

203 **Liquid to solid transition triggers the formation of fibrils and inhibits HuNoV GII.4 RdRp**
204 **activity**

205 To study the dynamics of protein molecules during the maturation of the RdRp condensates,
206 we monitored the material properties of the condensates for 12h using FRAP. In initial experiments,
207 the FRAP data revealed a complete fluorescence recovery (98 %) with a half-life ($t_{1/2}$) of 53.3 ± 2.1
208 s, which decreased significantly with time (Fig. S5A and B). These condensates retained liquid-like
209 properties for about 4 h and then transformed into gel-like or solid-like condensates. The increased
210 rigidity and reduced dynamicity of protein molecules within the condensates suggest that, over

211 time, these condensates change from liquid-like to solid-like, likely driven by the aggregation of
212 proteins. We investigated whether changing the fluidity of the condensates had any effect on the
213 enzymatic activity of RdRp molecules. As described in the above section, we performed the RNA
214 polymerization assay of RdRp post 12 h of incubation at 37 °C. The results indicate that the
215 reduction in the condensate's fluidity is proportional to the enzymatic activity (Fig. S5C). Negative
216 staining transmission electron microscopy of the phase separated samples after 12 h of incubation
217 at 37 °C showed fibrillar structures of varying lengths (Fig. S5D). Surprisingly, these fibrils have
218 amyloid-like characteristics, such as binding to amyloid-specific dyes thioflavin T (ThT) (Fig. S5E)
219 and Congo red (CR) (Fig. S5F). Such a transformation from liquid-like to solid-like amyloid fibrils
220 might provide a mechanism to regulate viral replication.

221 **GII.4 infected HIE cells show RdRp containing phase separated condensates.**

222 To investigate the formation of these condensates in the context of virus infection, we
223 infected HIEs with GII.4 HuNoV and performed immunofluorescence microscopy using anti-RdRp
224 antibody at different time points post-infection. The microscopy images show that RdRp was
225 initially diffuse and, with time, started forming discrete spherical condensates (Fig. 5A), which
226 gradually increased in size. Since these virus-infected cells needed to be fixed and permeabilized
227 for immunolabeling, we could not perform live cell imaging, including FRAP and fusion
228 experiments. In lieu of this, we examined the sensitivities of these condensates towards the aliphatic
229 alcohol 1,6-hexanediol (1,6 HD). The infected cells (24h post-infection) were treated with 5% (v/v)
230 1,6 HD (added to the cell culture medium) for 5 min and fixed with methanol. The cells were dual
231 immunolabeled with anti-RdRp antibody and anti-VP1 antibody (to detect the level of infection).
232 The confocal images of the 1,6 HD treated HIEs exhibit a reduction in the number of visible
233 condensates as compared to the untreated cells, indicating the dissolution of these condensates (Fig.
234 5B), suggesting their liquid-like nature. Together, these findings provide evidence that the observed
235 condensates in the virus infected HIEs harboring RdRp are formed via LLPS.

236 **Condensates in virus infected HIEs are RFs**

237 To determine if the condensates observed in the virus infected HIEs are the sites for viral
238 replication, we examined the colocalization of the RdRp with the replicative intermediate dsRNA.
239 Virus-infected HIEs were fixed, immunostained by antibodies against both GII.4 RdRp and dsRNA
240 and imaged using confocal microscopy. Colocalization of dsRNA with RdRp in the condensates
241 (Fig. 6A) was found, suggesting that these condensates are RFs. We further examined the
242 condensates for the presence of VPg, another critical component of the replication machinery
243 [44], using antibodies against both RdRp and VPg (Fig. 6B). Similar results were obtained when

244 purified RdRp was mixed with ssRNA and VPg (Fig. S6 A and B respectively) The images show
245 the coalescence of RdRp and VPg in these condensates. Together, these results strongly suggest
246 that these condensates are sites for viral replication.

247 **RdRp condensates are associated with markers for Golgi and ER**

248 Previous studies on picornaviruses, murine noroviruses, and other positive sense RNA
249 viruses have suggested a possible association of the RFs with membranes [18, 57]·[58, 59]. To
250 identify the association of any membrane components in the condensates formed during virus
251 infection, we examined the localization of various cellular membrane markers, including *trans*-
252 Golgi body (GalT), *cis*-Golgi body (GM130), ER (calnexin), *cis/medial*-Golgi body (Giantin), and
253 lysosomes (LAMP1) with RdRp marker. In contrast to GalT, which showed clear colocalization
254 with RdRp (Fig. 7A), no colocalization was detected with GM130, calnexin (Fig.s 7B and C),
255 Giantin, and LAMP1 (Fig. S7A and B). These results suggest that HuNoVs recruit membranes
256 derived from late compartments within the secretory pathway, especially *trans*-Golgi bodies, with
257 some specificity. We also investigated if any of the HuNoV nonstructural proteins with a membrane
258 binding domain, such as p41 (NS3), which is an NTPase and viral helicase and considered to be
259 critical for viral replication [60], is associated with the RdRp condensates. We performed these
260 experiments in HEK293T cells by co-transfecting RdRp-eGFP and p41-iRFP. The confocal
261 imaging of these cells shows that p41 co-localizes with RdRp, suggesting that RdRp condensates
262 can sequester membrane proteins involved in viral replication (Fig. S7C).

263

264 **Discussion**

265 In addition to their demonstrated role in regulating various cellular functions, biomolecular
266 condensates formed via LLPS are strongly implicated in forming viral RFs/inclusion bodies [13,
267 15-17]. For example, in the case of negative-sense RNA viruses, the involvement of LLPS in the
268 formation of inclusion bodies, which are the sites for viral genome replication, has been extensively
269 studied [13, 15, 16, 61]. The viroplasms formed during rotavirus infection, the genome replication
270 and sub-particle assembly sites, are considered biomolecular condensates formed by the
271 nonstructural proteins NSP5 and NSP2 [17]. In the case of SARS-CoV-2, the N protein undergoes
272 LLPS and sequesters components of the viral replication machinery [62]. Although RFs during
273 HuNoV infection are not yet described, distinct RFs are observed in the case of murine NoV
274 infection [57]; however, the involvement of LLPS in these RFs is not explored. In this study, we
275 show that purified RdRp of GII.4 HuNoV undergoes phase separation to create liquid-like, dynamic
276 condensates that contain a protein-rich, dense, yet highly mobile environment. Our studies further

277 suggest that these condensates observed in GII.4 HuNoV-infected HIEs are spherical, grow over
278 time, and are sensitive to 1,6 HD treatment, suggesting their liquid-like nature. We posit that these
279 condensates are the sites for viral replication, as they contain the replicative intermediate dsRNA
280 and necessary replication components RdRp and VPg. Bioinformatics analysis shows that RdRps
281 of almost all the norovirus genogroups have a high propensity to form LLPS (Fig. S8), suggesting
282 that LLPS formation by RdRp may be a common phenomenon in the Norovirus genera.

283 **Unique aspects of HuNoV GII.4 RdRp induced LLPS – initiating a hub for viral replication**

284 Typically, cellular or viral proteins require additional client proteins, crowding agents, or
285 RNA to phase separate under physiological conditions [35, [17]]. For example, up to 50 μM of the
286 SARS-CoV-2 N protein does not phase separate but adding 1 μM poly U significantly promotes
287 the phase separation [17]. Similarly, 35 μM NSP5 of rotavirus does not phase separate by itself; but
288 requires the presence of NSP2 or poly-arginine for phase separation [35]. In contrast, GII.4 RdRp
289 does not require any other viral protein or RNA for phase separation. It can phase separate at 5 μM
290 by itself and at 500 nM by adding a molecular crowding agent. Another interesting result, which
291 may have implications for viral replication, is that RdRp undergoes LLPS at pHs ranging from 5 to
292 9. , Also at pH 5, the minimum concentration of RdRp to form LLPS is reduced from 5 μM to 500
293 nM. This property may be of relevance considering that virus infection can alter the intracellular
294 pH [50-52]. The ability of RdRp to readily induce LLPS under various protein concentrations and
295 buffer conditions while remaining enzymatically active supports the idea that during viral infection
296 it likely initiates the formation of a sustainable platform for efficient replication.

297 **HuNoV RFs are liquid-like condensates**

298 Our experiments in HuNoV-infected HIEs strongly suggest that the condensates observed
299 during viral infection with liquid-like properties are the sites for viral replication as both the
300 replicative intermediate dsRNA and the viral nonstructural protein VPg colocalize with RdRp in
301 these condensates. VPg is a critical protein involved in viral replication and translation of viral
302 proteins. A recent study on murine NoV suggested that apart from its priming function, VPg can
303 physically interact with RdRp and enhance its polymerization activity [44].

304 A question that has to be considered while discussing the RFs as phase separated
305 condensates in positive-sense RNA viruses is whether they are associated with the membrane or
306 membrane components. Although not unequivocally demonstrated [63, 64], earlier studies on
307 picorna-like viruses [65] and murine noroviruses have suggested that RFs are associated with
308 intracellular membranes and vesicular structures [18, 57],[58, 59]. The formation of LLPS as a
309 potential hub or a driving force for forming the RFs does not exclude the incorporation or the

310 association of membrane-anchored proteins and lipids. Recent studies have implied such an
311 association could reduce the critical concentration for inducing LLPS and further for forming
312 microdomains within the membrane-associated condensates [66-68]. Our studies with membrane
313 markers in HuNoV infected HIEs show colocalization of RdRp with the *trans-Golgi* marker galT
314 in the condensates. The markers for other membrane components like *cis*/*medial*-Golgi (GM130),
315 ER (calnexin), cis/medial-Golgi body (Giantin), and lysosomes (LAMP1) show very little or no
316 association with RdRp in the condensates. In positive-sense RNA viruses, particularly the
317 picornavirus superfamily, the protein (s) involved in the biogenesis of the RFs usually contain a
318 domain that associates with the membrane or interacts with another viral protein that anchors it to
319 a cellular membrane, thereby creating a vesicular (membrane-associated) replication organelle [18,
320 19]. Our results in HEK293T cells show the sequestration of p41 (NS3), a membrane-anchored
321 protein with RNA helicase activity [60] to the RdRp condensates, leading to the possibility that p41
322 acts as a bridge between RdRp and the membranous component of replication complex. Further
323 studies are required to address the possible co-existence of phase separated condensates in the
324 context of vesicular structures in the replication of HuNoV and other picorna-like viruses.

325 **A mechanism to resolve the translation-replication conundrum?**

326 The formation of the RFs via LLPS in positive-sense RNA viruses may have a distinct advantage,
327 as has been recently suggested [69]. In positive sense RNA viruses, genomic RNA serves as the
328 basis for both translation by the ribosomes, which is processed from the 5' to the 3' end, and
329 replication by the RdRp from the 3' to the 5' end. These two processes running in opposite
330 directions pose a conundrum for the replication of these viruses, as previously recognized [70]. The
331 process of phase separation could provide an elegant solution for resolving this conflict by isolating
332 the newly synthesized RdRp capable of sequestering the replication components from interfering
333 with ribosomal translation. In the case of HuNoVs, RdRp, as we suggest, triggers the biogenesis
334 of phase separated RFs; however, in other positive-sense RNA viruses, it is quite possible that
335 another viral protein that is essential for replication could trigger this process by undergoing LLPS,
336 and then recruit the RdRp into the condensates.

337 **Liquid-to-solid transition as a regulatory mechanism**

338 Another common phenomenon of biomolecular condensates is the transition from liquid to
339 solid state over time. The FRAP analysis of the GII.4 RdRp condensates over time shows a lower
340 diffusion rate of the RdRp molecules in the condensates. Consistent with this observation, TEM
341 imaging of the RdRp incubated at 37 °C overnight demonstrated the formation of fibrils.
342 Interestingly, these fibrils bind to amyloid-specific dyes such as ThT and CR, indicating their

343 amyloid-like nature. RdRps of several picornaviruses also form similar fibrillar structures [71, 72],
344 although whether they exhibit amyloid-like properties is still unknown. We also observed that
345 under these conditions, the enzymatic activity of RdRp is significantly reduced supporting the
346 notion that the transition from liquid to solid state is plausibly a mechanism for regulating
347 replication. This could be the reason why all of the puncta are not dissolved by 5% 1,6HD, and do
348 not show colocalization of RdRp with dsRNA and VPg (Fig.s 5B and 6), as some of them may have
349 transitioned to the solid-like phase. Another possibility is that these amyloid-like fibrils may have
350 a role in inducing cell toxicity, as shown in the case of amyloid-like fibrils formed by the NS11
351 protein of SARS-CoV-2 [73].
352 In summary, our study reveals a previously unknown property of HuNoV RdRp in forming
353 biomolecular condensates as platforms for genome replication. In addition to exhibiting all the
354 properties for inducing the formation of LLPS in vitro, we have shown that RdRp also readily
355 undergoes LLPS in a cellular environment that resembles the condensates observed in virus-
356 infected HIEs strongly implicating RdRp in initiating and sustaining the viral RFs during HuNoV
357 infection. Our bioinformatics analysis suggests that this indeed may be a common phenomenon in
358 most noroviruses. The implication of RdRp in forming RFs also opens new targets for designing
359 antivirals for HuNoV infections, which remains a serious threat in children and
360 immunocompromised patients. Formation phase separated condensates as replication hubs may
361 perhaps be a necessary mechanism in the positive-sense RNA viruses, whether initiated by the
362 RdRp or other viral proteins, to effectively segregate the otherwise conflicting translation and
363 replication events.
364

365 **Materials and Methods**

366 **Cloning, expression, and purification of proteins**

367 Codon-optimized RdRp and VPg genes of HuNoV GII.4 Sydney strain (GenBank: AFV08794.1)
368 were synthesized and cloned in the pET28a vector for bacterial expression by Genscript U.S.A. Inc
369 with an N-terminal 6x His-tag to aid in the purification of both proteins. For mammalian expression
370 HuNoV GII.4 Sydney strain (GenBank: AFV08794.1) RdRp was cloned with eGFP on C-terminal,
371 VPg with mCherry on N-terminal, p41 with iRFP on N-terminal in pcDNA3.1(+) by Genscript
372 U.S.A. Inc. The N-terminal truncation, i.e., GII.4 RdRp-NΔ51 for bacterial expression were also
373 generated by Genscript U.S.A. Inc. For the over-expression of proteins, the plasmids containing the
374 desired genes were transformed into *E coli* BL21 (DE3) cells. Protein expression was induced by
375 the addition of 0.3 mM isopropyl β-D-1-thiogalactopyranoside at OD_{600} ~0.6. Cells were allowed

376 to express the protein at 18 °C for 16h with constant shaking at 200 rpm. Cells were harvested by
377 centrifugation at 4000xg for 30 min at 4 °C and the pellet was re-suspended in lysis buffer (20 mM
378 Tris-HCl pH 7.5, 250 mM NaCl, 5 mM imidazole, benzonase nuclease, and a cocktail of protease
379 inhibitors) followed by cell disruption using a microfluidizer. The supernatant was collected after
380 centrifugation at 18,000xg for 45 min at 4 °C. The protein was purified by affinity chromatography
381 using Ni-NTA agarose (Qiagen) resin followed by his tag cleavage by TEV protease and gel
382 filtration using Superdex 200 Increase 10/300 GL column (G.E. Healthcare) in 20 mM Tris-HCl
383 pH 7.5, 150 mM NaCl and 2 mM DTT. All the target proteins GII.4 RdRp, GII.4 RdRp-NΔ51, and
384 GII.4 VPg were purified using the above-mentioned protocol to a purity of >95% as judged by
385 SDS-PAGE and Coomassie blue stain.

386 **Analytical ultracentrifugation**

387 AUC experiments were carried out as previously described [74] with minor modifications. Briefly
388 sedimentation velocity experiments of 10 μM GII.4 RdRp were carried out using a Beckman-
389 Coulter XL-A analytical ultracentrifuge with a TiAn60 four-hole rotor and two-channel epon
390 centerpieces (12 mm) at 40,000 rpm at 22 °C. Absorbance scans were recorded at 280 nm at 1 min
391 intervals.

392 **Protein crystallization**

393 Crystallization screenings for GII.4 RdRp (10 mg/ml) were carried out by hanging-drop vapor
394 diffusion using the Mosquito crystallization robot (TTP LabTech) and imaged using Rock Imager
395 (Formulatrix) at 20 °C. The protein was crystallized under the conditions 0.3 M Sodium Iodide, 0.1
396 M Sodium Acetate: HCl, pH 4.5, 22.5 % (v/v) PurePEGs Cocktail. Crystals were flash-frozen
397 directly in liquid nitrogen.

398 **Structure determination and refinement**

399 X-ray Diffraction data for GII.4 RdRp was collected on APS beamline17-ID. Diffraction data were
400 processed with IMOSFLM as implemented in the CCP4 suite [75]. The structure of NV RdRP
401 (PDB ID: 4LQ3) was used as a search model for molecular replacement (MR) using PHASER. The
402 atomic model, including the side chain atoms, was then subjected to iterative cycles of refinement
403 using PHENIX and further model building using COOT based on the difference maps [76, 77].
404 Data collection and refinement statistics following the final refinement cycle are given in
405 Supplementary Table 1.

406 **SEC-SAXS data collection and processing**

407 The SEC-SAXS data for HuNoV GII.4 RdRp (5mg/ml, monomer) was collected at the SIBYLS
408 beamline 12.3.1 at the Advanced Light Source facility. The X-ray wavelength was fixed to λ =

409 1.127 Å, and the distance between the sample and the detector was set to 2100 mm, resulting in
410 scattering vectors (q) spanning from 0.01 to 0.4 Å−1. RdRp (60 µl) sample was prepared in running
411 buffer composed of 20 mM HEPES at pH 7.5, 150 mM NaCl, and 0.1% β-mercaptoethanol. The
412 Shodex KW803 column was equilibrated with the same running buffer, running at a flow rate of
413 0.5 ml/min. Each sample, consisting of 55 µl, was injected into the SEC column, and X-ray
414 exposures lasting 3 seconds were continuously recorded for over 30 minutes. Buffer subtraction
415 was performed using SCÅTTER (https://bl1231.als.lbl.gov/scatter/), and the resulting curves were
416 merged for subsequent Guinier analysis, Dimensionless Kratky plots, and P(r) plot computations.

417 **Solution structure modeling**

418 The crystal structure of RdRp (PDB ID: 8TUF) was used as a template for rigid body modeling.
419 Minimal molecular dynamic simulations were performed on the flexible N-terminal regions within
420 the structure to investigate the conformational space adopted by RdRp using BILBOMD [47]. This
421 approach involved storing a single conformational state approximately every 100 ps, yielding a
422 total of 10,000 conformers varying in Rg and Dmax values for subsequent SAXS fitting and
423 multistate validation [78]. Initially, scattering profiles from all 10,000 models were computed,
424 followed by genetic algorithm-selection operations to refine the selection to the most suitable
425 models. Finally, experimental scattering profiles from each construct were compared with
426 theoretical scattering profiles of the chosen atomistic models generated by BILBOMD, utilizing
427 FOXS [79].

428 **Light scattering measurements**

429 Light scattering measurements of GII.4 RdRp was carried out on a FlexStation3 plate reader
430 (Molecular Devices) using a 96-well flat bottom plate (Fisher Scientific) by measuring absorbance
431 at 350 nm at 37 °C at a regular interval of 2 min. Different concentrations of GII.4 RdRp (0.5, 1, 5,
432 10, 25 µM) were screened at varying concentrations of PEG3350 (0, 5, 10, 20%), pH (5.0, 6.0, 7.5,
433 and 9.0) and salt (NaCl) (0, 150, 300, 500, and 750 mM).

434 **Fluorescence labeling of proteins**

435 For microscopic visualization of condensates, GII.4 RdRp and GII.4 RdRp-NΔ51were labeled with
436 Atto-488 and GII.4 VPg was labeled with Atto-647N dye. For labeling an Atto 488 protein labeling
437 kit (Sigma-Aldrich, 38371) and an Atto 647N protein labeling kit (Sigma-Aldrich, 76508) were
438 used. The manufacturer's provided protocol was used. Briefly, 8 mg/ml RdRp, RdRp-NΔ51, and 6
439 mg/ml VPg were dialyzed in sodium bicarbonate buffer solution, pH 9.5 (provided with kit). Then
440 the protein solution was transferred to a vial containing the reactive dye dissolved in 20 µl sodium
441 bicarbonate buffer and incubated the reaction mixture for 2 h at room temperature while gently

442 stirring and protecting the vial from light. For the separation of protein-dye-conjugates from free
443 dye, the manufacturer's provided gel filtration columns were used to achieve good separation of
444 the protein-dye-conjugates from the excess free dye (size exclusion limit: 5 kDa). The protein-dye-
445 conjugates were eluted in phosphate buffer, pH 7.5 provided with the kit.

446 **Confocal microscopy**

447 Protein mixtures of 1% labeled and 99% unlabeled proteins were made at a concentration of 10
448 μM. An aliquot (15 μl) of the protein mixture was spotted onto 15 mm depression slides and
449 sandwiched with an 18 mm coverslip followed by sealing of the edges of the coverslip with
450 commercially available nail polish and allowed to phase separate at 37 °C for 45 min. The
451 condensates were visualized by Nikon A1R-s confocal microscope with 40X- air objective and 1
452 Airy unit aperture.

453 Different concentrations of GII.4 RdRp (0.5, 1, 5, 10, 25 μM) were screened at varying
454 concentration of PEG3350 (0, 5, 10, 20 %), pH (5.0, 6.0, 7.5, and 9.0) and salt (NaCl) concentration
455 (0, 150, 300, 500, and 750 mM) using a Yokogawa CV8000 high throughput spinning confocal
456 imaging platform with 60x/1.0 water immersion objective lens. Four fields of views with multiple
457 Z planes were captured.

458 **Far-UV circular dichroism (CD) measurements**

459 Far-UV CD measurements of RdRp and RdRp-NΔ51 were carried out using Circular Dichroism
460 Spectroscopy (J-1500, Jasco), using a 1-mm path-length quartz cuvette. Data were recorded using
461 a final protein concentration of 8 μM proteins in 20 mM sodium phosphate buffer pH 7.5. The
462 spectra were averaged over three scans and were blank subtracted. The spectra were then processed
463 using Spectra Manager™ CDPro (Jasco) and plotted using Origin 2018.

464 **Negative-stain transmission electron microscopy (EM)**

465 GII.4 RdRp (10 μM, 50 μl) was incubated at 37 °C at a constant shaking at 200 rpm for 20 s after
466 every 2 min for a period of 12 h. For preparing negatively stained grids, 3 μl of the GII.4 RdRp
467 (diluted 10 times) was adsorbed onto a glow-discharged grid carbon-coated grid (CF200-CU; EMS)
468 for 60 s. The grid was blotted with Whatman's filter paper 541 and washed twice with deionized
469 water with intermittent blotting. The grid was further stained with three drops of 2 % uranyl acetate
470 with intermittent blotting to remove the residual stain. The grids were air-dried and imaged at room
471 temperature using a JEM 2100 transmission electron microscope operated at 200 keV (JEOL)
472 equipped with a LaB6 filament, 3kx4k Direct Electron Detector (DE12) and a Gatan 4kx4k CCD
473 at the cryo-EM core facility, Baylor college of Medicine. The images were recorded at 15k using a
474 low-dose procedure and a defocus range of −1 to −4 μm.

475 **GII.4 HuNoV infection of HIE monolayers**

476 Five day differentiated monolayers were infected with 1 x 10^7 GE of GII.4 stool filtrate in CMGF(-
477) for 1 h at 37 ºC. After washing two times with CMGF(-), the HIEs were incubated at 37 °C for
478 different time points (8-20 h). The cells were fixed with 100% chilled methanol for 20 min at room
479 temperature. The cells were incubated with 1:150 dilution of rabbit anti-RdRp [80] in 5 % BSA
480 PBS at 4 °C overnight. The cells were washed three times with PBS containing 0.1 % Triton X-100
481 and incubated with goat anti-rabbit 488 (#A-11008, ThermoFisher Scientific) overnight at 4 º C to
482 visualize the viral proteins. The cells were washed three times, and the nuclei were stained with 4,
483 6-diamidino-2-phenylindole (DAPI) (300 nM) followed by subsequent Z-stack images captured
484 using a Nikon A1 confocal microscope. For treatment with 1,6 HD, the cells post-infection 20 h
485 were treated with 5% 1,6 HD which was added to the cell culture medium for 5 min and fixed with
486 100% chilled methanol as described above. The cells were incubated with 1:150 dilution of rabbit
487 anti-RdRp [80] and 1:500 dilution of guinea pig VP1antibody in 5 % BSA PBS at 4 °C overnight
488 and washed and imaged as described above. For dual leveling experiment of RdRp with dsRNA,
489 VPg and membrane components, the antibodies used are mouse anti-dsRNA (Millipore Sigma),
490 anti-VPg (in house produced), anti-GalT (Abcam), anti-GM130 (Abcam), anti- calnexin (Abcam),
491 anti- Giantin, and anti- LAMP1(Santa Cruz Biotechnology).

492 **Mammalian cell line and expression**

493 HEK293T (ATCC, CRL-3216) (2 x 10^5 cells per well) were seeded in µ-Slide 8-well glass-bottom
494 plates (Ibidi) in DMEM media and incubated at 37 °C for 24 h. Cells were then transfected with
495 respective plasmids and incubated 37 °C. After 24 h, the cells were stained with Hoechst 33342
496 diluted in FluoroBRITE DMEM at a concentration of 1 mg/mL, incubated for 30 min at 37 °C.

497 **Fluorescence recovery after photobleaching (FRAP)**

498 FRAP studies were performed using a laser scanning confocal microscope (Nicon-A1R-s) with a
499 40x air objective. A circular area encompassing an entire condensate was bleached with a 404 nm
500 laser (100 %) for 20 iterations and recovery was recorded for 300 s at 10 s intervals. For in vitro
501 FRAP study, 15 µl RdRp (10 µM) was spotted onto 15 mm depression slides and sandwiched with
502 18 mm coverslip followed by sealing of the edges of the coverslip with commercially available nail
503 polish and allowed to phase separate at 37 °C. After droplet formation was confirmed, the slides
504 containing the condensates were subjected to FRAP experiments at various time points as indicated
505 in the respective sections. For live cell FRAP, the bleaching of ROI was performed at 70 % laser
506 power for 20 iterations and recovery was recorded for 500 s at 15 s interval. The images were
507 corrected for laser bleaching by selecting a fluorescent region outside the ROI.

508 **Estimation of light phase and dense phase concentration**

509 The concentrations of the dense phase and light phase were estimated using centrifugation by
510 following a previously described protocol [56]. For dense phase concentration estimation, 100 µl
511 RdRp (10 µM) was incubated at 37 °C for 45 min and centrifuged at ~ 25,000 x g at 37 °C for 15
512 min. After carefully removing the supernatant in several steps, the pure dense phase (~ 2 µL) was
513 re-suspended in 100 µl of the denaturation buffer (6M guanidine hydrochloride, 20 mM sodium
514 phosphate). The absorbance at 280 nm was recorded using nanodrop. The light phase concentration
515 was estimated from the absorbance of the supernatant at 280 nm.

516 **Fluorescence-based activity assay for GII.4 RdRp**

517 GII.4 RdRp activity was measured using a real-time fluorescence-based assay, which uses SYTO9,
518 a fluorescence dye that specifically binds dsRNA but not ssRNA template molecules. Reactions
519 were performed in individual wells of black 96-well flat-bottom plates (costar). The standard
520 reaction contained GII.4 RdRp (5 µM), 20 mM Tris-HCl pH 7.5, 5 mM MgCl2, 2.5 mM MnCl2,
521 40 µg/mL polyC, 5 U RNAseOUT (invitrogen) and 0.25 µM SYTO9 (Sigma-Aldrich). The reaction
522 was initiated by the addition of 300 µM GTP and the fluorescence was recorded after every 2 min
523 over 60 min at 30 °C using a plate reader FlexStation3 (Molecular devices). For measuring the
524 activity of RdRp after incubation at 37 °C, the incubated RdRp (10 µM) was centrifuged at
525 20,000xg for 20 min. The supernatant was removed, and pallet was mixed thoroughly, and activity
526 was measured using the same protocol as described above. To measuring the activity of RdRp in
527 the condensates the same reaction was setup in 96 Well glass bottom plates (Cellvis) and the
528 fluorescence was recorded after every 20 min over 180 min at 37 °C using using a Yokogawa
529 CV8000 high throughput spinning confocal imaging platform with 60x/1.0 water immersion
530 objective lens. Four fields of views with multiple Z planes were captured.

531 **Thioflavin T fluorescence assays**

532 10 µM GII.4 RdRp was mixed with 10-fold molar excess of ThT and fluorescence intensity was
533 measured using excitation wavelength of 440 nm and emission wavelength of 482 nm using a plate
534 reader FlexStation3 (Molecular devices) at constant temperature of 37 °C and readings were
535 acquired every 2 min with continuous orbital shaking between reads over a period of 24 h. The top
536 of the each well was sealed using adhesive tape to minimize the rate of evaporation. Three
537 independent experiments were performed in triplicates and the bars represent the standard
538 deviation.

539 **Congo red binding assay**

540 CR dye solution was prepared by mixing 7 mg/mL dye in and passed through a 0.22 µm filter prior
541 to use. The spectrum of CR (5 µL in 1 mL 20 mM Tris-HCl pH 7.5, 150 mM NaCl, and 5 mM
542 DTT) was recorded between 400 and 700 nm at room temperature (negative control). 10 µM RdRp
543 was incubated with C.R. for 12 h at 37 °C and the spectrum was recorded between 400 and 700 nm
544 a plate reader FlexStation3 (Molecular devices)
545

546 **References and Notes:**

547 1. Brangwynne, C.P., et al., *Germline P granules are liquid droplets that localize by*
548 *controlled dissolution/condensation.* Science, 2009. **324**(5935): p. 1729-32.
549 2. Feric, M., et al., *Coexisting Liquid Phases Underlie Nucleolar Subcompartments.* Cell,
550 2016. **165**(7): p. 1686-1697.
551 3. Boeynaems, S., et al., *Protein Phase Separation: A New Phase in Cell Biology.* Trends
552 Cell Biol, 2018. **28**(6): p. 420-435.
553 4. Dignon, G.L., R.B. Best, and J. Mittal, *Biomolecular Phase Separation: From Molecular*
554 *Driving Forces to Macroscopic Properties.* Annu Rev Phys Chem, 2020. **71**: p. 53-75.
555 5. Zhang, H., et al., *Liquid-liquid phase separation in biology: mechanisms, physiological*
556 *functions and human diseases.* Sci China Life Sci, 2020. **63**(7): p. 953-985.
557 6. Shin, Y. and C.P. Brangwynne, *Liquid phase condensation in cell physiology and disease.*
558 Science, 2017. **357**(6357).
559 7. Kroschwald, S., et al., *Promiscuous interactions and protein disaggregases determine the*
560 *material state of stress-inducible RNP granules.* Elife, 2015. **4**: p. e06807.
561 8. Banani, S.F., et al., *Biomolecular condensates: organizers of cellular biochemistry.* Nat
562 Rev Mol Cell Biol, 2017. **18**(5): p. 285-298.
563 9. Pak, C.W., et al., *Sequence Determinants of Intracellular Phase Separation by Complex*
564 *Coacervation of a Disordered Protein.* Mol Cell, 2016. **63**(1): p. 72-85.
565 10. Maharana, S., et al., *RNA buffers the phase separation behavior of prion-like RNA binding*
566 *proteins.* Science, 2018. **360**(6391): p. 918-921.
567 11. Netherton, C.L. and T. Wileman, *Virus factories, double membrane vesicles and*
568 *viroplasm generated in animal cells.* Curr Opin Virol, 2011. **1**(5): p. 381-7.
569 12. Novoa, R.R., et al., *Virus factories: associations of cell organelles for viral replication*
570 *and morphogenesis.* Biol Cell, 2005. **97**(2): p. 147-72.
571 13. Nikolic, J., et al., *Negri bodies are viral factories with properties of liquid organelles.* Nat
572 Commun, 2017. **8**(1): p. 58.

573 14. Heinrich, B.S., et al., *Phase Transitions Drive the Formation of Vesicular Stomatitis Virus*
574 *Replication Compartments.* mBio, 2018. **9**(5).
575 15. Zhou, Y., et al., *Measles Virus Forms Inclusion Bodies with Properties of Liquid*
576 *Organelles.* J Virol, 2019. **93**(21).
577 16. Galloux, M., et al., *Minimal Elements Required for the Formation of Respiratory Syncytial*
578 *Virus Cytoplasmic Inclusion Bodies In Vivo and In Vitro.* mBio, 2020. **11**(5).
579 17. Geiger, F., et al., *Liquid-liquid phase separation underpins the formation of replication*
580 *factories in rotaviruses.* EMBO J, 2021. **40**(21): p. e107711.
581 18. Harak, C. and V. Lohmann, *Ultrastructure of the replication sites of positive-strand RNA*
582 *viruses.* Virology, 2015. **479-480**: p. 418-33.
583 19. Reid, C.R., A.M. Airo, and T.C. Hobman, *The Virus-Host Interplay: Biogenesis of +RNA*
584 *Replication Complexes.* Viruses, 2015. **7**(8): p. 4385-413.
585 20. Jack, A., et al., *SARS-CoV-2 nucleocapsid protein forms condensates with viral genomic*
586 *RNA.* bioRxiv, 2021.
587 21. Wang, J., et al., *SARS-CoV-2 nucleocapsid protein undergoes liquid-liquid phase*
588 *separation into stress granules through its N-terminal intrinsically disordered region.* Cell
589 Discov, 2021. **7**(1): p. 5.
590 22. Chen, H., et al., *Liquid-liquid phase separation by SARS-CoV-2 nucleocapsid protein and*
591 *RNA.* Cell Res, 2020. **30**(12): p. 1143-1145.
592 23. Perdikari, T.M., et al., *SARS-CoV-2 nucleocapsid protein phase-separates with RNA and*
593 *with human hnRNPs.* EMBO J, 2020. **39**(24): p. e106478.
594 24. Savastano, A., et al., *Nucleocapsid protein of SARS-CoV-2 phase separates into RNA-rich*
595 *polymerase-containing condensates.* Nat Commun, 2020. **11**(1): p. 6041.
596 25. Wang, S., et al., *Targeting liquid-liquid phase separation of SARS-CoV-2 nucleocapsid*
597 *protein promotes innate antiviral immunity by elevating MAVS activity.* Nat Cell Biol,
598 2021. **23**(7): p. 718-732.
599 26. Lin, W. and P.D. Nagy, *Co-opted cytosolic proteins form condensate substructures within*
600 *membranous replication organelles of a positive-strand RNA virus.* New Phytol, 2024.
601 27. Kirk, M.D., et al., *World Health Organization Estimates of the Global and Regional*
602 *Disease Burden of 22 Foodborne Bacterial, Protozoal, and Viral Diseases, 2010: A Data*
603 *Synthesis.* PLoS Med, 2015. **12**(12): p. e1001921.
604 28. Mortality, G.B.D. and C. Causes of Death, *Global, regional, and national age-sex specific*
605 *all-cause and cause-specific mortality for 240 causes of death, 1990-2013: a systematic*

606 *analysis for the Global Burden of Disease Study 2013.* Lancet, 2015. **385**(9963): p. 117-
607 71.
608 29. Bartsch, S.M., et al., *Global Economic Burden of Norovirus Gastroenteritis.* PLoS One,
609 2016. **11**(4): p. e0151219.
610 30. Mattison, C.P., C.V. Cardemil, and A.J. Hall, *Progress on norovirus vaccine research:*
611 *public health considerations and future directions.* Expert Rev Vaccines, 2018. **17**(9): p.
612 773-784.
613 31. Lopman, B.A., et al., *The Vast and Varied Global Burden of Norovirus: Prospects for*
614 *Prevention and Control.* PLoS Med, 2016. **13**(4): p. e1001999.
615 32. Chhabra, P., et al., *Updated classification of norovirus genogroups and genotypes.* J Gen
616 Virol, 2019. **100**(10): p. 1393-1406.
617 33. van Beek, J., et al., *Molecular surveillance of norovirus, 2005-16: an epidemiological*
618 *analysis of data collected from the NoroNet network.* Lancet Infect Dis, 2018. **18**(5): p.
619 545-553.
620 34. Yang, Y., et al., *Genetic and phenotypic characterization of GII-4 noroviruses that*
621 *circulated during 1987 to 2008.* J Virol, 2010. **84**(18): p. 9595-607.
622 35. Campillay-Veliz, C.P., et al., *Human Norovirus Proteins: Implications in the Replicative*
623 *Cycle, Pathogenesis, and the Host Immune Response.* Front Immunol, 2020. **11**: p. 961.
624 36. Vongpunsawad, S., B.V. Venkataram Prasad, and M.K. Estes, *Norwalk Virus Minor*
625 *Capsid Protein VP2 Associates within the VP1 Shell Domain.* J Virol, 2013. **87**(9): p.
626 4818-25.
627 37. Ayyar, B.V., et al., *CLIC and membrane wound repair pathways enable pandemic*
628 *norovirus entry and infection.* Nat Commun, 2023. **14**(1): p. 1148.
629 38. Ettayebi, K., et al., *Replication of human noroviruses in stem cell-derived human*
630 *enteroids.* Science, 2016. **353**(6306): p. 1387-1393.
631 39. Alvarado, G., et al., *Broadly cross-reactive human antibodies that inhibit genogroup I and*
632 *II noroviruses.* Nat Commun, 2021. **12**(1): p. 4320.
633 40. Saar, K.L., et al., *Learning the molecular grammar of protein condensates from sequence*
634 *determinants and embeddings.* Proc Natl Acad Sci U S A, 2021. **118**(15).
635 41. Xue, B., et al., *PONDR-FIT: a meta-predictor of intrinsically disordered amino acids.*
636 Biochim Biophys Acta, 2010. **1804**(4): p. 996-1010.

637 42. Meszaros, B., G. Erdos, and Z. Dosztanyi, *IUPred2A: context-dependent prediction of*
638 *protein disorder as a function of redox state and protein binding.* Nucleic Acids Res,
639 2018. **46**(W1): p. W329-W337.
640 43. Deval, J., et al., *Structure(s), function(s), and inhibition of the RNA-dependent RNA*
641 *polymerase of noroviruses.* Virus Res, 2017. **234**: p. 21-33.
642 44. Lee, J.H., et al., *Insight Into the Interaction Between RNA Polymerase and VPg for*
643 *Murine Norovirus Replication.* Front Microbiol, 2018. **9**: p. 1466.
644 45. Shaik, M.M., et al., *Norovirus RNA-dependent RNA polymerase: A computational study of*
645 *metal-binding preferences.* Proteins, 2017. **85**(8): p. 1435-1445.
646 46. Smertina, E., et al., *Calicivirus RNA-Dependent RNA Polymerases: Evolution, Structure,*
647 *Protein Dynamics, and Function.* Front Microbiol, 2019. **10**: p. 1280.
648 47. Pelikan, M., G.L. Hura, and M. Hammel, *Structure and flexibility within proteins as*
649 *identified through small angle X-ray scattering.* Gen Physiol Biophys, 2009. **28**(2): p.
650 174-89.
651 48. Lin, Y., et al., *Toxic PR Poly-Dipeptides Encoded by the C9orf72 Repeat Expansion*
652 *Target LC Domain Polymers.* Cell, 2016. **167**(3): p. 789-802 e12.
653 49. Liu, X., et al., *Time-dependent effect of 1,6-hexanediol on biomolecular condensates and*
654 *3D chromatin organization.* Genome Biol, 2021. **22**(1): p. 230.
655 50. Moore, L.L., D.A. Bostick, and R.F. Garry, *Sindbis virus infection decreases intracellular*
656 *pH: alkaline medium inhibits processing of Sindbis virus polyproteins.* Virology, 1988.
657 **166**(1): p. 1-9.
658 51. Ciriolo, M.R., et al., *Loss of GSH, Oxidative Stress, and Decrease of Intracellular pH as*
659 *Sequential Steps in Viral Infection*.* Journal of Biological Chemistry, 1997. **272**(5): p.
660 2700-2708.
661 52. Okda, F.A., et al., *Interplay between H1N1 influenza a virus infection, extracellular and*
662 *intracellular respiratory tract pH, and host responses in a mouse model.* PLoS One, 2021.
663 **16**(5): p. e0251473.
664 53. Paiz, E.A., et al., *Beta turn propensity and a model polymer scaling exponent identify*
665 *intrinsically disordered phase-separating proteins.* J Biol Chem, 2021. **297**(5): p. 101343.
666 54. Saez-Alvarez, Y., et al., *Development of a fluorescence-based method for the rapid*
667 *determination of Zika virus polymerase activity and the screening of antiviral drugs.* Sci
668 Rep, 2019. **9**(1): p. 5397.

669 55. Yin, W., et al., *Structural basis for inhibition of the SARS-CoV-2 RNA polymerase by*
670 *suramin.* Nat Struct Mol Biol, 2021. **28**(3): p. 319-325.
671 56. Agarwal, A., et al., *An intrinsically disordered pathological prion variant Y145Stop*
672 *converts into self-seeding amyloids via liquid-liquid phase separation.* Proc Natl Acad Sci
673 U S A, 2021. **118**(45).
674 57. Hyde, J.L., et al., *Mouse norovirus replication is associated with virus-induced vesicle*
675 *clusters originating from membranes derived from the secretory pathway.* J Virol, 2009.
676 **83**(19): p. 9709-19.
677 58. Zhang, Y., X. Cao, and D. Li, *Architecture of viral replication factories.* Oncotarget,
678 2015. **6**(31): p. 30439-40.
679 59. Zhang, Z., et al., *Host Lipids in Positive-Strand RNA Virus Genome Replication.* Front
680 Microbiol, 2019. **10**: p. 286.
681 60. Li, T.F., et al., *Human Norovirus NS3 Has RNA Helicase and Chaperoning Activities.* J
682 Virol, 2018. **92**(5).
683 61. Hirai, Y., K. Tomonaga, and M. Horie, *Borna disease virus phosphoprotein triggers the*
684 *organization of viral inclusion bodies by liquid-liquid phase separation.* Int J Biol
685 Macromol, 2021. **192**: p. 55-63.
686 62. Chau, B.A., et al., *Liquid-liquid phase separation of nucleocapsid proteins during SARS-*
687 *CoV-2 and HIV-1 replication.* Cell Rep, 2022. **42**(1): p. 111968.
688 63. Paul, D. and R. Bartenschlager, *Architecture and biogenesis of plus-strand RNA virus*
689 *replication factories.* World J Virol, 2013. **2**(2): p. 32-48.
690 64. Wolff, G., et al., *Double-Membrane Vesicles as Platforms for Viral Replication.* Trends
691 Microbiol, 2020. **28**(12): p. 1022-1033.
692 65. Ahola, T., *New Phylogenetic Grouping of Positive-Sense RNA Viruses Is Concordant with*
693 *Replication Complex Morphology.* mBio, 2019. **10**(4).
694 66. Ditlev, J.A., *Membrane-associated phase separation: organization and function emerge*
695 *from a two-dimensional milieu.* J Mol Cell Biol, 2021. **13**(4): p. 319-324.
696 67. Miller, E.J., et al., *Divide and conquer: How phase separation contributes to lateral*
697 *transport and organization of membrane proteins and lipids.* Chem Phys Lipids, 2020.
698 **233**: p. 104985.
699 68. Zhao, Y.G. and H. Zhang, *Phase Separation in Membrane Biology: The Interplay between*
700 *Membrane-Bound Organelles and Membraneless Condensates.* Dev Cell, 2020. **55**(1): p.
701 30-44.

69. Sagan, S.M. and S.C. Weber, *Let's phase it: viruses are master architects of biomolecular condensates.* Trends Biochem Sci, 2023. **48**(3): p. 229-243.
70. Gamarnik, A.V. and R. Andino, *Switch from translation to RNA replication in a positive-stranded RNA virus.* Genes Dev, 1998. **12**(15): p. 2293-304.
71. Lyle, J.M., et al., *Visualization and functional analysis of RNA-dependent RNA polymerase lattices.* Science, 2002. **296**(5576): p. 2218-22.
72. Bentham, M., et al., *Formation of higher-order foot-and-mouth disease virus 3D(pol) complexes is dependent on elongation activity.* J Virol, 2012. **86**(4): p. 2371-4.
73. Bhardwaj, T., et al., *Amyloidogenic proteins in the SARS-CoV and SARS-CoV-2 proteomes.* Nat Commun, 2023. **14**(1): p. 945.
74. Kumar, D., et al., *2.7 A cryo-EM structure of rotavirus core protein VP3, a unique capping machine with a helicase activity.* Sci Adv, 2020. **6**(16): p. eaay6410.
75. Winn, M.D., et al., *Overview of the CCP4 suite and current developments.* Acta Crystallogr D Biol Crystallogr, 2011. **67**(Pt 4): p. 235-42.
76. Adams, P.D., et al., *PHENIX: a comprehensive Python-based system for macromolecular structure solution.* Acta Crystallogr D Biol Crystallogr, 2010. **66**(Pt 2): p. 213-21.
77. Emsley, P., et al., *Features and development of Coot.* Acta Crystallogr D Biol Crystallogr, 2010. **66**(Pt 4): p. 486-501.
78. Schneidman-Duhovny, D. and M. Hammel, *Modeling Structure and Dynamics of Protein Complexes with SAXS Profiles.* Methods Mol Biol, 2018. **1764**: p. 449-473.
79. Schneidman-Duhovny, D., et al., *FoXS, FoXSDock and MultiFoXS: Single-state and multi-state structural modeling of proteins and their complexes based on SAXS profiles.* Nucleic Acids Res, 2016. **44**(W1): p. W424-9.
80. Karandikar, U.C., et al., *Detection of human norovirus in intestinal biopsies from immunocompromised transplant patients.* J Gen Virol, 2016. **97**(9): p. 2291-2300.

Acknowledgments

This research used resources of the Advanced Photon Source, a U.S. Department of Energy (DOE) Office of Science user facility operated for the DOE Office of Science by Argonne National Laboratory under Contract No. DE-AC02-06CH11357. We acknowledge SIBYLS beamline 12.3.1 at the Advanced Light Source facility for SEC-SAXS data collection. Imaging for this project was supported by the Center for Advanced Microscopy and Image Informatics (CAMII, CPRIT

RP170719) and the Integrated Microscopy Core at Baylor College of Medicine (funding from NIH (DK56338, CA125123, ES030285, S10OD030414). We also acknowledge the CryoEM Core at Baylor College of Medicine for all the TEM experiments. We acknowledge the Protein Characterization Unit, Protein and Monoclonal Antibody Production Core, BCM. GK was supported by the Cancer Prevention and Research Institute of Texas grant RR160029 (to Xiaodong Cheng, MD Anderson Cancer Center).

Funding: This work was supported by National Institutes of Health grant P01 AI057788 (BVVP) and Robert Welch Foundation grant Q1279 (BVVP).

Author contributions:

Conceptualization: BVVP, SK

Methodology: SK, RA, BVA, GK, SS

Investigation: SK, RA, BVA,GK

Visualization: SK, BVA, GK, FS

Supervision: BVVP, MKE, SEC, FS, JP

Writing original draft: BVVP, SK

Writing review & editing: BVVP, SK, RA, BVA, GK, SS, SEC, MKE, FS, JP

Competing interests: The authors declare that they have no competing interests.

Data and materials availability: All data needed to evaluate the conclusions in the paper are present in the paper and/or the Supplementary Materials.

Figures

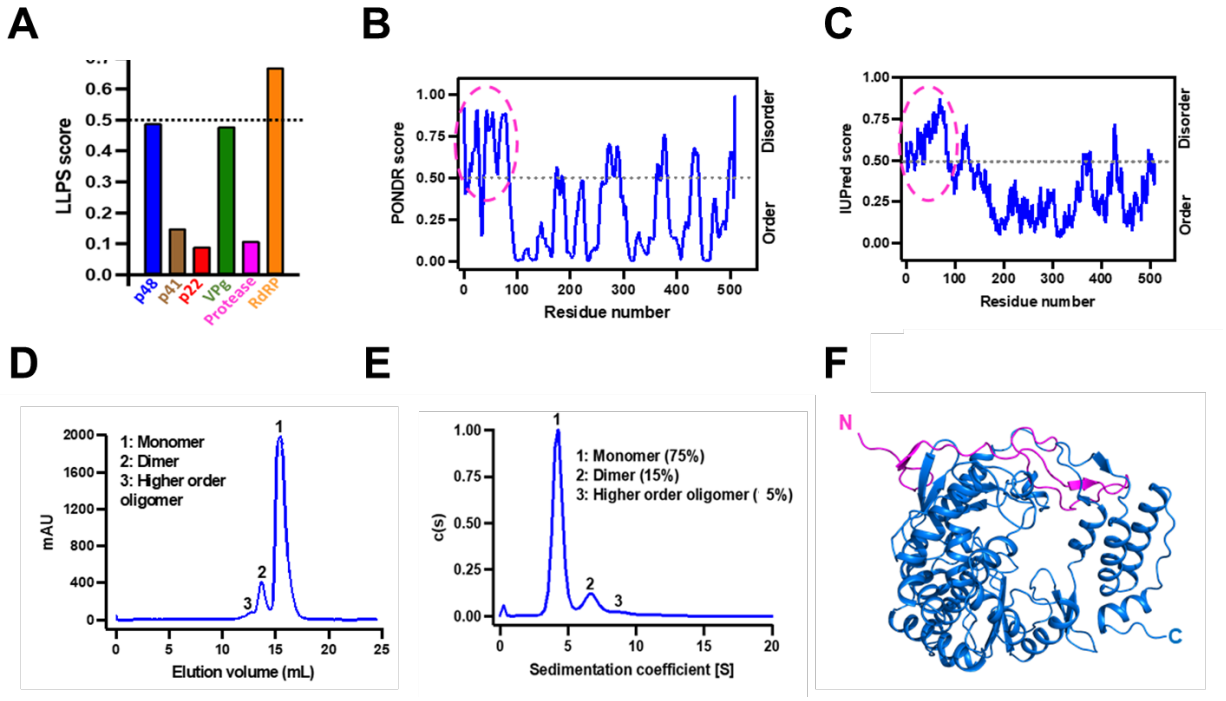

Figure 1. GII.4 RdRp has the required properties to undergo LLPS. (A) Bioinformatics analysis of the primary amino acid sequences of all nonstructural proteins of HuNoV GII.4 to predict LLPS propensity using DeePhase. The dotted black line indicates the threshold LLPS score

of proteins to undergo LLPS. (B-C) The disorder prediction of GII.4 RdRp primary amino acid sequence using bioinformatics tools (B) PONDR (C) IUPred2. The dotted black line in both panels indicates the threshold disorder score and the dotted pink circle shows the predicted disordered N-terminal region. (D-E) The oligomeric state of GII.4 RdRp analyzed using (D) size exclusion chromatography and (E) sedimentation velocity analytical ultracentrifugation. (F) A cartoon representation of the crystal structure of GII.4 RdRp showing the disordered/flexible N-terminal region colored in pink.

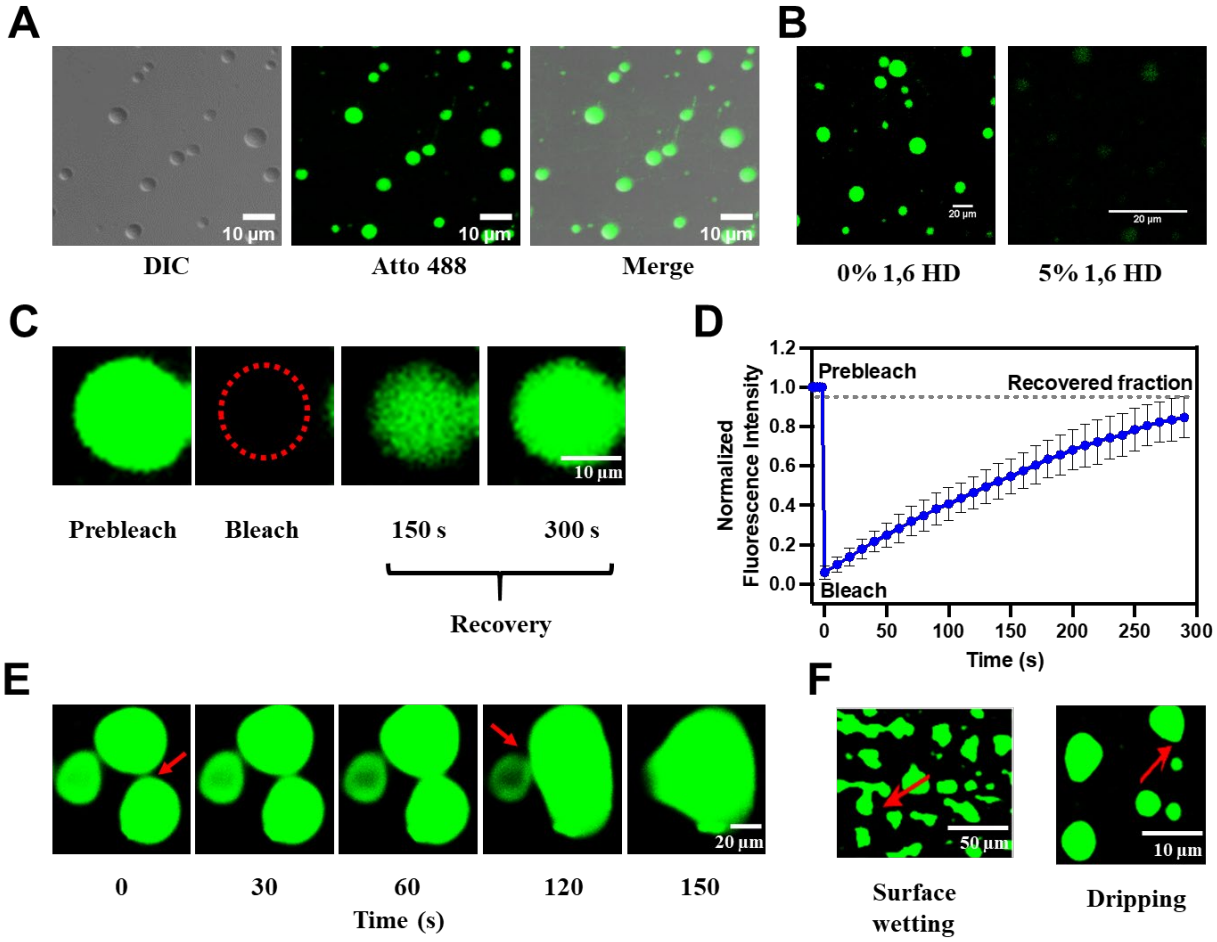

Figure 2. HuNoV GII.4 RdRp undergoes LLPS in vitro. (A) Differential interference contrast (DIC) and confocal images of phase separated RdRp (1 % Atto 488 labeled and 99 % unlabeled). Phase separated RdRp possesses liquid-like properties. (B) Effect of 1,6 hexanediol on LLPS of RdRp. (C) FRAP of RdRp in condensate photobleached at the position indicated by the red circle. (D) The graph shows the recovery curve where normalized fluorescence intensity was plotted

808 against time. (E) Time-lapse images of RdRp condensates exhibit the formation of larger
809 condensates by the fusion of smaller condensates over time. The red arrows indicate the site of
810 fusion. (F) Surface wetting and dripping using confocal microscopy. The red arrows indicate the
811 position of surface wetting and dripping.
812
813
814
815

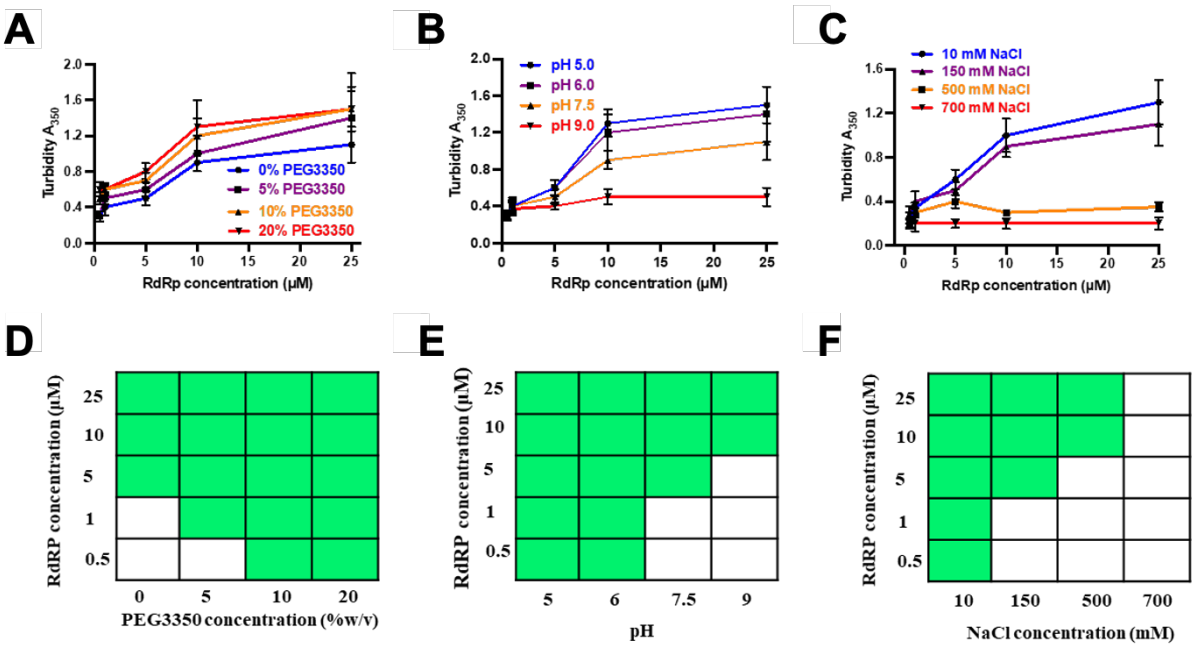

816

817 **Figure 3. Phase separation of GII.4 RdRp is modulated by PEG3350 concentration, pH, and**
818 **salt concentration.** Effect of (A) protein and PEG3350 concentrations, (B) protein concentrations
819 and pH, (C) protein and salt concentrations on the phase separation of RdRp was assessed by
820 measuring the turbidity of the samples at OD 350 nm. (D-F) A phase diagram of RdRp at (D)
821 protein and PEG3350 concentrations, (E) at protein concentrations and pH, at (F) protein and salt
822 concentrations constructed from the confocal microscopy images. The green boxes indicate LLPS
823 (condensate state), and the white boxes indicate no LLPS (soluble state).
824
825
826
827

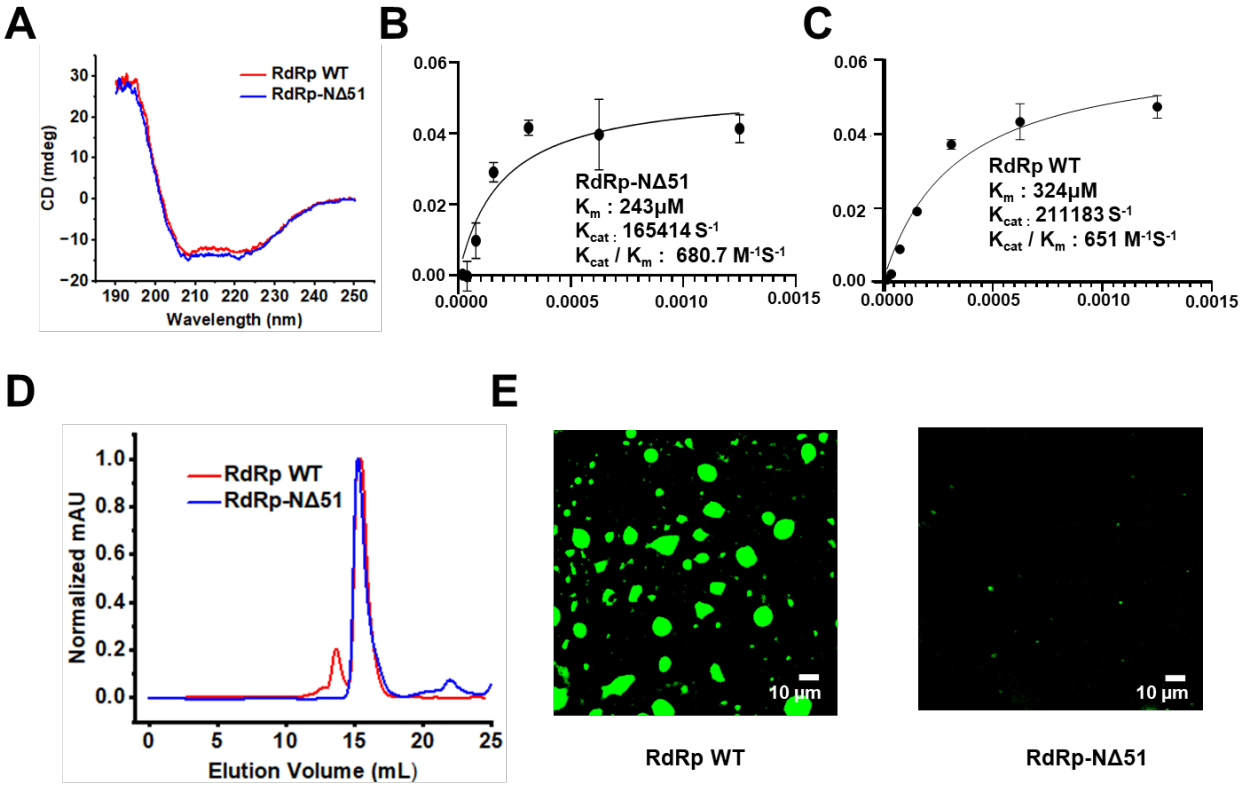

Figure 4. Effect of N-terminal deletion on phase separation of GII.4 RdRp. Purified RdRp WT and RdRp-NΔ51 were analyzed by **(A)** CD spectroscopy **(B and C)** Enzyme activity **(D)** Size exclusion chromatography and **(E)** confocal microscopy.

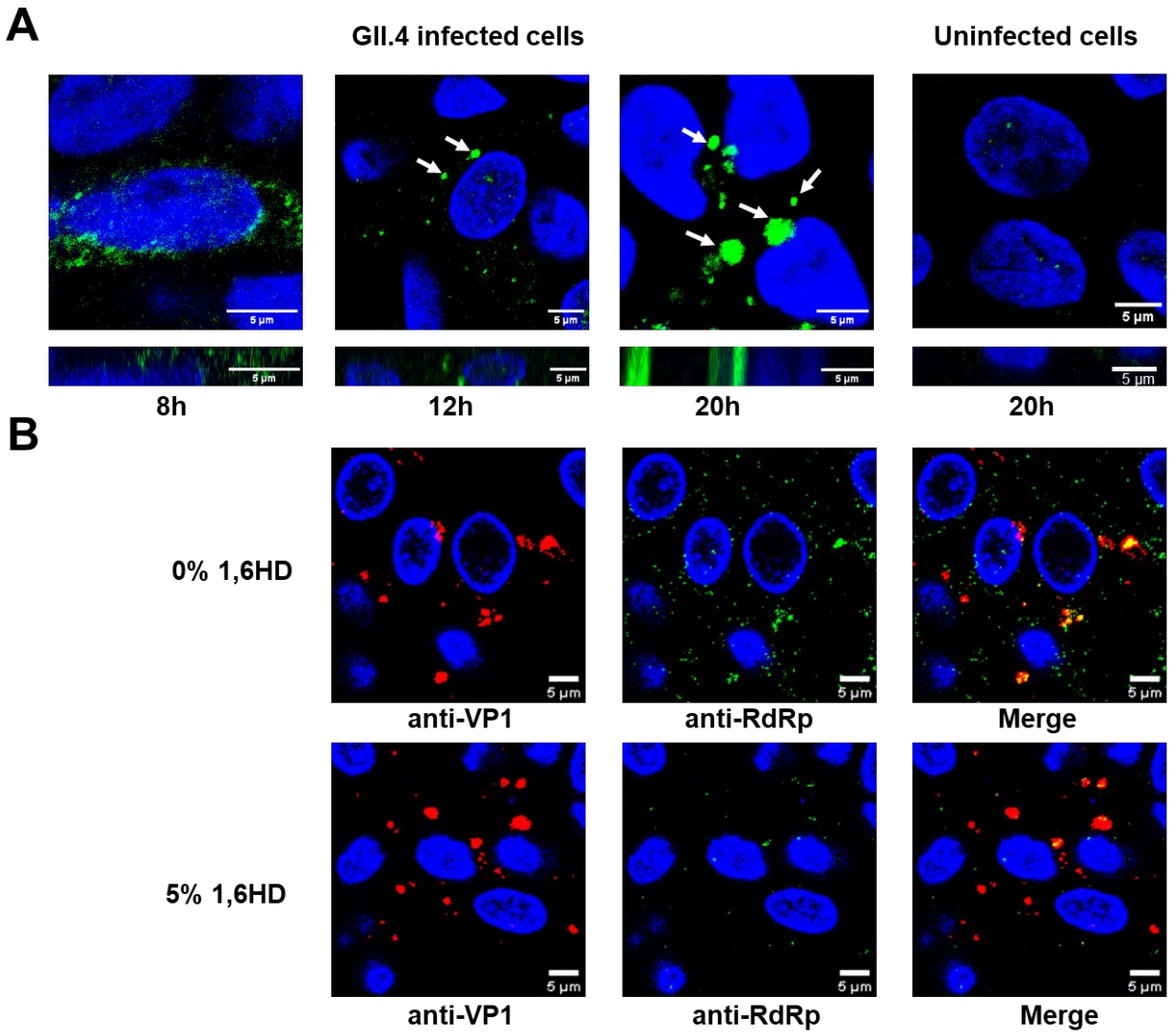

Figure 5. RdRp forms liquid-like condensates in GII.4 infected HIEs. (A) Confocal microscopy images of GII.4 HuNoV-infected HIEs at different time points post infection showing condensate formation detected by anti-RdRp antibody (green). Uninfected HIEs were used as negative control. Red arrows indicate the position of representative condensates. **(B)** Effect of 1,6 Hexanediol on the condensates formed in the GII.4 HuNoV-infected HIEs suggesting their liquid like nature.

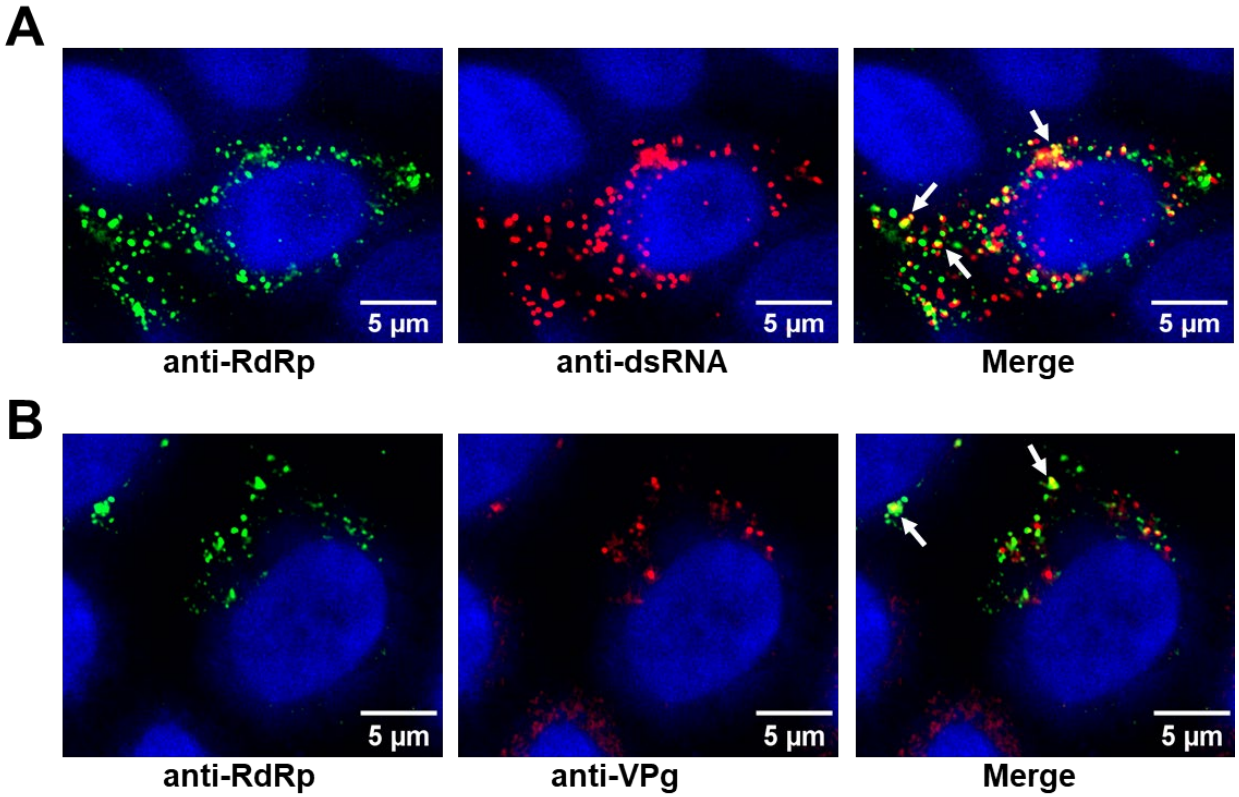

844

845 **Figure 6. GII.4 RdRp condensates are the sites for viral replication.** Confocal images of the
846 GII.4 HuNoV-infected HIEs showing **(A)** Colocalization (yellow) of dsRNA (red) and
847 RdRp(green) detected by respective antibodies **(B)** Colocalization (yellow) of VPg (red) and
848 RdRp(green) detected by respective antibodies. In both the panels white arrows indicate the site of
849 colocalization.

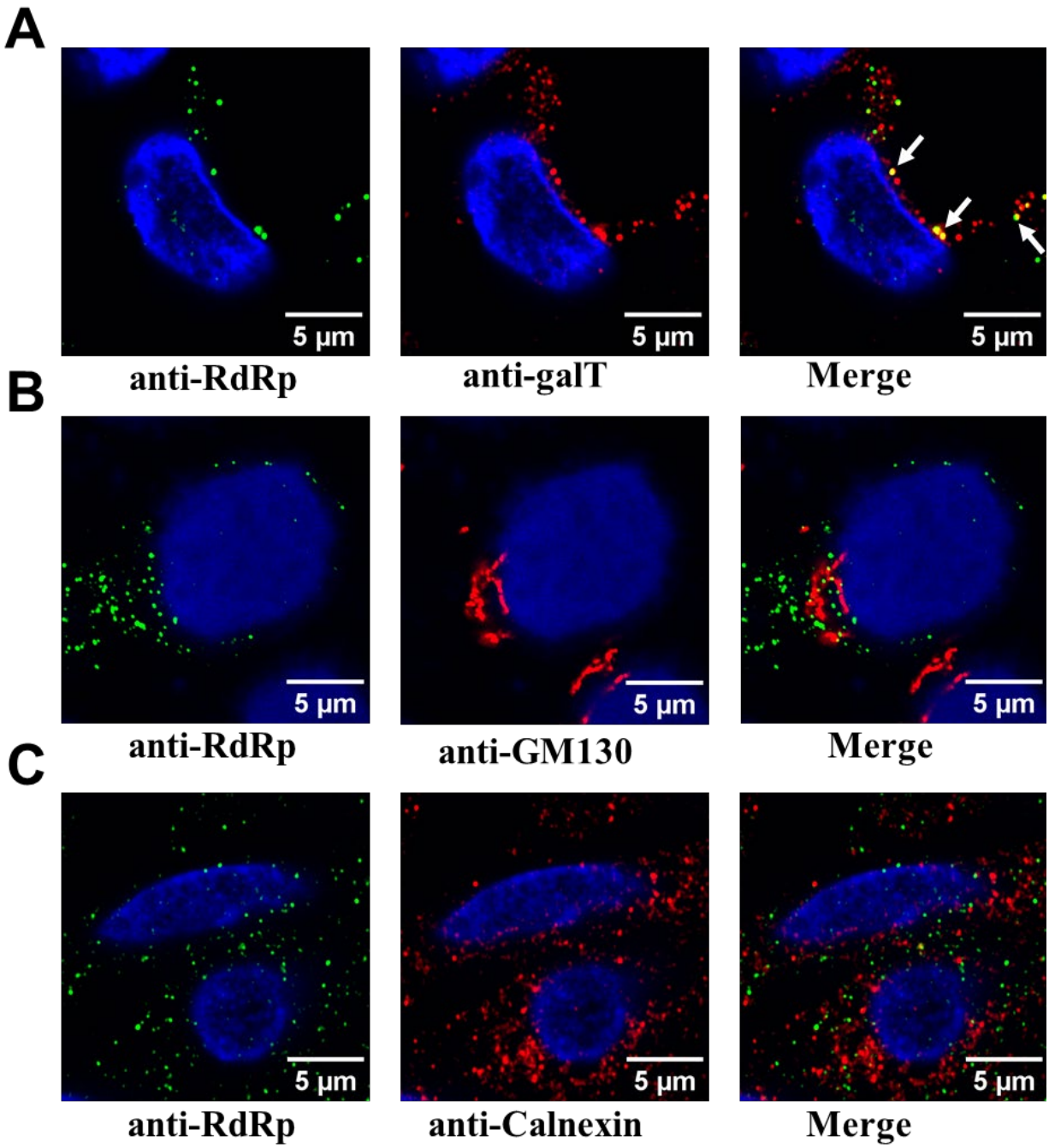

Figure 7. Association of RdRp condensates with membrane markers. GII.4 HuNoV-infected HIEs were fixed and dual labeled with markers for RdRp (green) and various cellular membrane markers (red) **(A)** for the *trans*-Golgi (GalT) **(B)** *cis* Golgi (GM130) **(C)** ER (calnexin).

Supplementary Material includes 1 table and 8 Figures with legends